Signed-distance function based non-rigid registration of image series with varying image intensity

Kateřina Škardová, Tomáš Oberhuber, Jaroslav Tintěra, Radomir Chabiniok

Manuscript submitted to
AIMS' Journals
Volume **X**, Number **0X**, XX **200X**

doi:10.3934/xx.xx.xx.xx

pp. **X–XX**

SIGNED-DISTANCE FUNCTION BASED NON-RIGID REGISTRATION OF IMAGE SERIES WITH VARYING IMAGE INTENSITY

Kateřina Škardová[*,a], Tomáš Oberhuber[a], Jaroslav Tintěra[b] and Radomír Chabiniok[a,c,d,e]

[a]Department of Mathematics, FNSPE, Czech Technical University in Prague
Trojanova 13, 120 00 Prague, Czech Republic
[b]Department of Radiology, Institute for clinical and experimental medicine
Vídeňská 1958/9, Praha 4, 140 21, Czech Republic
[c] Inria, France
[d] LMS, Ecole Polytechnique, CNRS, Institut Polytechnique de Paris, France
[e] School of Biomedical Engineering & Imaging Sciences (BMEIS)
St Thomas' Hospital, King's College London, UK

(Communicated by the associate editor name)

Abstract. In this paper we propose a method for locally adjusted optical flow-based registration of multimodal images, which uses the segmentation of the object of interest and its representation by the signed-distance function (OF^{dist} method). We deal with non-rigid registration of the image series acquired by the Modiffied Look-Locker Inversion Recovery (MOLLI) magnetic resonance imaging sequence, which is used for a pixel-wise estimation of T_1 relaxation time. The spatial registration of the images within the series is necessary to compensate the patient's imperfect breath-holding. The evolution of intensities and a large variation of image contrast within the MOLLI image series, together with the myocardium of left ventricle (the object of interest) typically not being the most distinct object in the scene, makes the registration challenging. The paper describes all components of the proposed OF^{dist} method and their implementation. The method is then compared to the performance of a standard mutual information maximization-based registration method, applied either to the original image (MIM) or to the signed-distance function (MIM^{dist}). Several experiments with synthetic and real MOLLI images are carried out. On synthetic image with a single object, MIM performed the best, while OF^{dist} and MIM^{dist} provided better results on synthetic images with more than one object and on real images. When applied to signed-distance function of two objects of interest, MIM^{dist} provided a larger registration error (but more homogeneously distributed) compared to OF^{dist}. For the real MOLLI image series with left ventricle pre-segmented using a level-set method, the proposed OF^{dist} registration performed the best, as is demonstrated visually and by measuring the increase of mutual information in the object of interest and its neighborhood.

1. **Introduction.** Image registration [3] is defined as a geometrical aligning of two images of the same object taken at different times or captured by different imaging techniques. It is a challenging image processing task that is encountered in many

2010 *Mathematics Subject Classification.* Primary: 58F15, 58F17; Secondary: 53C35.

Key words and phrases. distance function, locally adjusted image registration, image segmentation, optical flow.

* Corresponding author: katerina.skardova@fjfi.cvut.cz.

fields such as remote sensing, biomedical imaging [10, 19], map matching and many others. The registration of two scenes is a necessary step for image processing tasks in the field of medical imaging, e.g. in compensation for patient's moving during data acquisition or in integration of data obtained by different imaging techniques.

The image acquisition by different modalities often means that not only the intensity but also the image contrast and texture do not match. However, the problem of varying intensities or contrast occurs also in registering the images from one source. An example of such a series is the image series acquired by the Modified Look-Locker Inversion Recovery (MOLLI) magnetic resonance imaging sequence, used for a pixel-wise estimation of T_1 relaxation times. The spatial registration of the images within the MOLLI series is necessary to compensate the patient's imperfect breath-holding. The main characteristics of the MOLLI image series are the evolution of intensities and large variation of the image contrast. In particular, the myocardium of left ventricle – the object of interest in the images – is often not the most distinct object in the scene, which makes the registration process challenging.

In [10] three main categories of registration methods are presented: *Landmark-*, *segmentation-* and *voxel property-based* methods. In the *landmark-based* registration methods, the alignment of images is obtained by registering a finite set of points – landmarks – detected in the source and target images. The landmarks should be accurately detectable in all registered images. They can either be detected manually based on knowledge of the scene or automatically based on some geometrical properties (e.g. points of curvature extrema, intersections, etc.). The set of detected points is sparse compared to the original image, which makes the registration process faster. However, as pointed out in [11], the heart exhibits less accurate anatomical and geometrical landmarks than for example brain, which limits the use of landmark-based registration methods on heart images. In the *segmentation-based* methods, the objects extracted from the source image are deformed to fit the objects in the target image. The segmentation is usually made semi-automatically. Finally, the *voxel property-based* methods use all information contained in the image without a reduction to the set of points or segmented objects by working directly with the image voxel values. This category of methods includes for instance the maximization of mutual information [9] and optical flow estimation [6] – the two methods on which the presented paper is based.

In this work, we propose a *segmentation-based* registration method based on representing the segmented objects by their signed-distance functions. The optical flow – traditionally a *voxel-property-based* registration method – is used for the signed-distance functions registration. The representation by the signed-distance maps excludes the effect of varying intensities and, additionally, captures all local deformations of the segmented objects. It is, therefore, a suitable representation of the segmented objects.

The level-set method used for segmentation of the objects of interest is described in Sections 2, the subsequent computation of the signed-distance function is described in Section 3. The optical flow method which is applied to the distance functions is introduced in Section 4. The numerical solution of the problem is described in Section 5. The experimental results and comparison of the proposed method with two other registration approaches are presented in Section 6.

2. **Segmentation of the myocardium.** The image segmentation is a process of dividing the image into several parts – the segments. In this work, the myocardium is segmented using the level-set method for edge detection. The result of this method is a closed smooth curve corresponding with the myocardium edge. The outer (epicardial) and subsequently the inner (endocardial) edge of the myocardium is detected and the myocardium is then defined as the area between these two curves.

2.1. **Mean-curvature motion of level sets.** The level-set methods are based on representing a dynamic curve $C(\theta)$ as a zero level set of a corresponding level-set function $\psi(\vec{x},\theta)$, i.e. $C(\theta) = \{\vec{x}$, such that $\tilde{\psi}(\vec{x},\theta) = 0\}$ [12]. We assume that the level-set function takes positive values on the exterior of curve $C(\theta)$ – denoted as $C(\theta)_{ext}$ – and negative values in the interior – denoted as $C(\theta)_{int}$, i.e.:

$$\begin{aligned} \tilde{\psi}(\vec{x},\theta) &= 0, \quad \forall \vec{x} \in C(\theta), \forall \theta \in [0,\infty), \\ \tilde{\psi}(\vec{x},\theta) &< 0, \quad \forall \vec{x} \in C(\theta)_{int}, \forall \theta \in [0,\infty), \\ \tilde{\psi}(\vec{x},\theta) &> 0, \quad \forall \vec{x} \in C(\theta)_{ext}, \forall \theta \in [0,\infty). \end{aligned} \tag{1}$$

The initial curve represented by $\tilde{\psi}_0(\vec{x})$ is placed around the object which is to be contoured. Then, by the evolution of the level-set function the curve is adapted to the contour of the object. During the evolution, the equation $\tilde{\psi}(\vec{x}(\theta),\theta) = 0$, $\forall \theta \in [0,\infty)$, has to be satisfied. Further, the equation describing the evolution of the level-set function [17] can be derived:

$$\frac{\partial \tilde{\psi}}{\partial \theta} + |\nabla \tilde{\psi}| V = 0, \tag{2}$$

where V denotes the magnitude of the velocity in the direction of the outer normal unit vector to the curve C. By setting V to a mean curvature of the curve C [2], i.e. $V = -\nabla \cdot \left(\frac{\nabla \tilde{\psi}}{|\nabla \tilde{\psi}|} \right)$, the level-set formulation of the mean-curvature flow is obtained:

$$\frac{\partial \tilde{\psi}}{\partial \theta} - |\nabla \tilde{\psi}| \nabla \cdot \left(\frac{\nabla \tilde{\psi}}{|\nabla \tilde{\psi}|} \right) = 0. \tag{3}$$

For theoretical and numerical reasons, $|\nabla \tilde{\psi}|$ is regularized as $|\nabla \tilde{\psi}|_\epsilon = \sqrt{\epsilon^2 + |\nabla \tilde{\psi}|^2}$ [2, 15]. In this work $\epsilon = 10^{-4}$ was used. The final form of the equation reads:

$$\begin{aligned} \frac{\partial \tilde{\psi}}{\partial \theta} - |\nabla \tilde{\psi}|_\epsilon \nabla \cdot \left(\frac{\nabla \tilde{\psi}}{|\nabla \tilde{\psi}|_\epsilon} \right) &= 0 \quad \text{on } \Omega \times (0, T_{fin}], \\ \tilde{\psi}(x,0) &= \tilde{\psi}_0(x) \quad \text{on } \Omega, \\ \nabla \tilde{\psi} \cdot \vec{n} &= 0 \quad \text{on } \partial\Omega \times (0, T_{fin}]. \end{aligned} \tag{4}$$

2.2. **Edge detection using mean-curvature flow.** In the image processing, edges are typically characterized by a large gradient of the image intensity. In an input image represented by image intensity function $I : \Omega \to [i_{\min}, i_{\max}]$, where Ω denotes the image domain and $[i_{\min}, i_{\max}]$ is the range of intensities, the edges can be detected based on the norm of image function gradient. For the application

in the edge detection, the level-set equation (3) is modified in the following way [1]:

$$\begin{aligned} \frac{\partial \tilde{\psi}}{\partial \theta} &= |\nabla \tilde{\psi}|_\epsilon g_0 \nabla \left(\frac{\nabla \tilde{\psi}}{|\nabla \tilde{\psi}|_\epsilon} \right) + \nabla \tilde{\psi} \cdot \nabla g_0, \quad \text{on } \Omega \times (0, T_{fin}], \\ \tilde{\psi}(x,0) &= \tilde{\psi}_0(x) \quad \text{on } \Omega, \\ \nabla \tilde{\psi} \cdot \vec{n} &= 0 \quad \text{on } \partial\Omega \times (0, T_{fin}], \end{aligned} \tag{5}$$

where function $g_0 = g_0(|\nabla I|)$ depends on the norm of the image gradient. We use function g_0 in the form $g_0(|\nabla I|) = 1/(1+K|\nabla I|^2)$, as proposed in [14]. The function g_0 controls the velocity of the propagation of the contour C defined by the level-set function $\tilde{\psi}$. In the regions with high values of $|\nabla I|$ (typically on the edges), the velocity is close to zero. The parameter K modifies the sensitivity to variations of image intensity. Its value depends on the image contrast. The position of the initial curve for the outer edge segmentation is set by the user. The initial condition for the inner edge segmentation is obtained by subtracting the constant from the signed-distance function of the segmented outer edge, which moves the zero level set inwards. The constant is also provided by the user.

For the application on real data, two preprocessing methods were used. First, the histogram equalization [20] was used for increasing the contrast in images. The method adjusts the distribution of the intensities in the histogram and spreads out the most frequent intensities. Secondly, for image smoothing, equation (4) was solved. The parameters of numerical solutions are specified in Section 6.

3. Signed-distance function.

A level-set function $\psi(\vec{x}) = \tilde{\psi}(\vec{x}, T_{fin})$ is obtained as a result of the segmentation process. It is, however, not a suitable representation of the segmented object, as one object might be represented by several level-set functions. Therefore, function $\tilde{\phi}$, which has the same zero level set as function ψ and additionally has the properties of the signed-distance function, is constructed. Only one signed-distance function exists for each segmented object and therefore it is a representation suitable for comparing the objects. Function $\tilde{\phi}$ with the characteristics described above is obtained by solving the following equation [18]:

$$\begin{aligned} \frac{\partial \tilde{\phi}}{\partial \theta} &= S(\psi) \left(1 - \left\| \nabla \tilde{\phi} \right\| \right) \quad \text{on } \Omega \times (0, T_{fin}), \\ \tilde{\phi}(x,0) &= \psi(x) \quad \text{on } \Omega, \\ \nabla \tilde{\phi} \cdot \vec{n} &= 0 \quad \text{on } \partial\Omega \times (0, T_{fin}), \end{aligned} \tag{6}$$

where function S is defined as smoothed sign function $S(\psi) = \psi/\sqrt{\psi^2 + \varepsilon^2}$. The shape representation by the signed-distance function is convenient as it distributes the information about contour C into the whole area Ω and thus enables the use of the optical flow registration method.

4. Optical flow based registration.

Optical flow [6] is a vector field containing the displacements that occur between the images of the same scene taken at times t and $t + \Delta t$.

Let us consider an image series represented by a time-dependent image function $I : \Omega \times T \to [i_{\min}, i_{\max}]$, where T represents the time interval during which the images were taken.

For the series of images, the optical flow is defined as a vector field $\vec{u}(\vec{x},t) = (u_1(\vec{x},t), u_2(\vec{x},t), t)$, where $u_i(\vec{x},t) : \Omega \times T \to \mathbb{R},\ i \in \{1,2\}$ denote the displacements in directions of axes x and y, respectively. To determine the optical flow, a rule for finding the correspondence between the points on images taken at time t and $t + \Delta t$ is needed. In most optical flow determining algorithms the correspondence is found based on a constancy assumption, which states that a certain value remains unchanged in time. The assumption frequently used for a single-modality registration is the *brightness constancy assumption*, according to which the intensity of each point remains the same in all images of the given series, i.e.:

$$I(x(t), y(t), t) = D, \quad \forall t \in T. \tag{7}$$

In the proposed method, the optical flow is applies to series of signed-distance functions. The object can be represented by signed-distance function in each image of the original image-sequence. This way we obtain time dependent signed-distance function $\phi(x,t)$. Specifically, from image $I_1(\vec{x}) = I(\vec{x}, t_1)$ we obtain $\psi_1(\vec{x}) = \tilde{\psi}_1(\vec{x}, T_{fin})$ by solving (5), subsequently we get $\tilde{\phi}_1(\vec{x}, T_{fin})$ as a solution of (6). Finally we assign $\phi(x, t_1) = \tilde{\phi}_1(\vec{x}, T_{fin})$.

The constancy is applied to the signed-distance function ϕ:

$$\phi(x(t), y(t), t) = D, \quad \forall t \in T. \tag{8}$$

In other words, we assume that the distance of a given point from the edge of the segmented object remains constant in time. The determined transformation is subsequently applied to the original source image.

From the registration point of view, it is not necessary to see the MOLLI sequence as a continuous evolution of the scene in time, as the deformations are independent of the ordering of the images. Instead, the sequence can be divided into several two-image subsequences, each containing the target and one of the source images. The time dimension is then neglected and we set the value $\Delta t = 1$ in each subsequence, for simplicity.

By total derivation of equation (8) we obtain the *optical flow constraint* equation:

$$\frac{\partial \phi}{\partial x} u_1 + \frac{\partial \phi}{\partial y} u_2 + \frac{\partial \phi}{\partial t} = 0, \tag{9}$$

where u_1 and u_2 denote x- and y-component of the displacements.

The variational approach is used to regularize the optical flow. All the assumptions on the vector field are therefore formulated as minimization problems. First, the following functional derived from the *optical flow constraint* is used:

$$E_{constancy}(u_1, u_2) = \int_\Omega \left(\frac{\partial \phi}{\partial x} u_1 + \frac{\partial \phi}{\partial y} u_2 + \frac{\partial \phi}{\partial t} \right)^2. \tag{10}$$

Two additional assumptions are stated on the displacement vector field to ensure the uniqueness of the solution: the assumption of smoothness and the assumption of minimal magnitude. These two assumptions, together with the constancy assumption, force the zero displacements in the areas with the constant values of image

function I. The final functional has the following form:

$$E(u_1,u_2) = \alpha \underbrace{\int_\Omega \left(\frac{\partial \phi}{\partial x}u_1 + \frac{\partial \phi}{\partial y}u_2 + \frac{\partial \phi}{\partial t}\right)^2}_{E_{constancy}} + \beta \underbrace{\int_\Omega q\left(\|\nabla u_1\|^2 + \|\nabla u_2\|^2\right)}_{E_{smoothness}} + \gamma \underbrace{\int_\Omega u_1^2 + u_2^2}_{E_{magnitude}}, \tag{11}$$

where $q\left(\|\nabla u_1\|^2 + \|\nabla u_2\|^2\right) = \sqrt{\epsilon + \|\nabla u_1\|^2 + \|\nabla u_2\|^2}$. The terms of functional (11) will be referred to as $E_{constancy}$, $E_{smoothness}$ and $E_{magnitude}$, respectively.

The domain of functional $E(u_1,u_2)$ is $W = W^{1,2}(\Omega) \times W^{1,2}(\Omega)$, where $W^{1,2}(\Omega)$ is the Sobolev space $W^{1,2}(\Omega) = \left\{u | u, D_x u, D_y u \in L^2(\Omega)\right\}$ [7]. The functions minimizing functional E on its domain are denoted as (u_1^*, u_2^*).

Functional $E(u_1,u_2)$ is convex and therefore satisfies the equation

$$\mathrm{d}E((u_1^*,u_2^*);(\theta_1,\theta_2)) = 0, \quad \forall (\theta_1,\theta_2) \in W, \tag{12}$$

where $\mathrm{d}E(u_1^*,u_2^*)$ is the Fréchet derivative of functional E at the point (u_1^*,u_2^*) [16]. Equation (12) is the necessary and sufficient condition for the functions (u_1^*,u_2^*) to be minimizers of the functional $E(u_1,u_2)$[16].

Using the *fundamental lemma of calculus of variations* [4] it can be proven that the minimizing functions (u_1^*,u_2^*) have to satisfy the following set of equations:

$$\begin{aligned}
&\alpha\left(\frac{\partial \phi}{\partial x}u_1^* + \frac{\partial \phi}{\partial y}u_2^* + \frac{\partial \phi}{\partial t}\right)\frac{\partial \phi}{\partial x} - \beta\nabla\cdot\left(q'(\|\nabla u_1^*\|^2 + \|\nabla u_2^*\|^2)\nabla u_1^*\right) + \gamma u_1^* = 0,\\
&\alpha\left(\frac{\partial \phi}{\partial x}u_1^* + \frac{\partial \phi}{\partial y}u_2^* + \frac{\partial \phi}{\partial t}\right)\frac{\partial \phi}{\partial y} - \beta\nabla\cdot\left(q'(\|\nabla u_1^*\|^2 + \|\nabla u_2^*\|^2)\nabla u_2^*\right) + \gamma u_2^* = 0.
\end{aligned} \tag{13}$$

The nonlinear set of equations (13) is solved using the method of steepest descend. The following set of partial differential equations is obtained:

$$\begin{aligned}
\frac{\partial u_1}{\partial \theta} &= -\alpha\left(\frac{\partial \phi}{\partial x}u_1 + \frac{\partial \phi}{\partial y}u_2 + \frac{\partial \phi}{\partial t}\right)\frac{\partial \phi}{\partial x}\\
&\quad + \beta\nabla\cdot\left(q'(\|\nabla u_1\|^2 + \|\nabla u_2\|^2)\nabla u_1\right) - \gamma u_1 \quad \text{on } \Omega\times(0,T_{fin}),
\end{aligned} \tag{14}$$

$$\begin{aligned}
\frac{\partial u_2}{\partial \theta} &= -\alpha\left(\frac{\partial \phi}{\partial x}u_1 + \frac{\partial \phi}{\partial y}u_2 + \frac{\partial \phi}{\partial t}\right)\frac{\partial \phi}{\partial y}\\
&\quad + \beta\nabla\cdot\left(q'(\|\nabla u_1\|^2 + \|\nabla u_2\|^2)\nabla u_2\right) - \gamma u_2 \quad \text{on } \Omega\times(0,T_{fin}),
\end{aligned} \tag{15}$$

$$\begin{aligned}
u_i|_{\theta=0} &= u_{i,0} \quad \text{on } \Omega,\ i=1,2\\
u_i &= 0 \quad \text{on } \partial\Omega\times(0,T_{fin}],\ i=1,2.
\end{aligned}$$

In the case of no prior knowledge about the initial vector field, the initial conditions $u_{1,0}, u_{2,0}$ are set to uniform value $\pm 0.1h$, where h is the spatial discretization step.

The diagram of the proposed method is shown in Figure 1. For the source image $I(\vec{x},t)$ and target image image $I(\vec{x},t+\Delta t)$, the object of interest is segmented by solving (5). The signed-distance functions $\tilde{\phi}_1(\vec{x},T_{fin})$ and $\tilde{\phi}_2(\vec{x},T_{fin})$ obtained from (6) are assigned to $\phi(x,t)$ and $\phi(x,t+\Delta t)$, respectively. Finally the optical flow is computed by solving (14), (15). By applying the transformation to the source signed-distance function $\phi(\vec{x},t)$, we obtain approximation of $\phi(\vec{x},t+\Delta t)$. Similarly,

by applying the transformation to the source image $I(\vec{x},t)$, we obtain approximation of the target image $I(\vec{x},t+\Delta t)$.

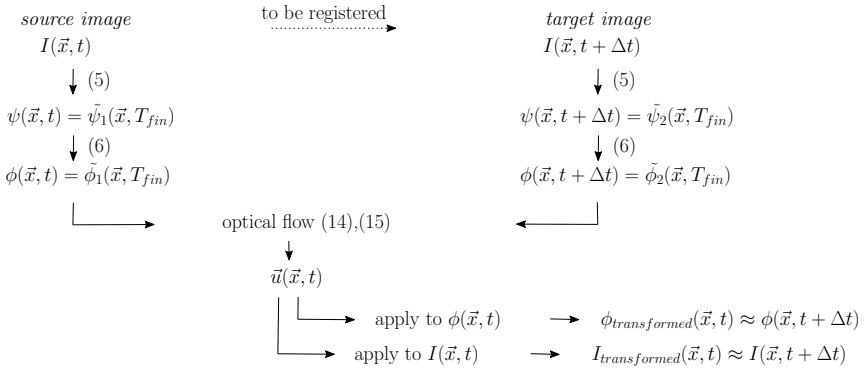

FIGURE 1. Diagram of the proposed method.

5. Numerical Solution.

5.1. Spatial Discretization and Approximation of Spatial Derivatives.

The complementary finite volume method described in [5, 8] is used for the spatial discretization. The digital image can be considered as a grid of pixels denoted by V:

$$V=\{(ih,(i+1)h)\times(jh,(j+1)h)\mid i=0,..,N_1-1,j=0,..,N_2-1\}, \qquad (16)$$

where $h=1/\max(N_1,N_2)$ is the spatial step. The individual volume elements of set V are denoted by $V_{i,j}=(ih,(i+1)h)\times(jh,(j+1)h)$. The centers of volume elements $V_{i,j}$ are denoted by $x_{i,j}=\left[\left(\frac{1}{2}+i\right)h,\left(\frac{1}{2}+j\right)h\right]$.

The set of volume elements and the central points are shown in Figure 2. The

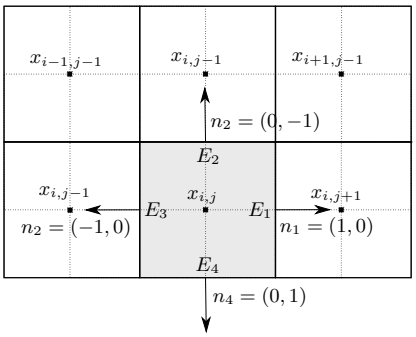

FIGURE 2. Volume elements and the central points.

finite differences are used to approximate the spatial derivatives of ϕ in optical flow method. The forward finite difference in direction x of function ϕ at point $x_{i,j}$ and time t_k is denoted by $\phi^k_{x;i,j}=(\phi^k_{i+1,j}-\phi^k_{i,j})/h$, the backward difference is denoted by $\overline{\phi}^k_{x;i,j}=(\phi^k_{i,j+1}-\phi^k_{i+1,j})/h$ and the central difference by $\dot{\phi}^k_{x;i,j}=(\phi^k_{i+1,j}-\phi^k_{i-1,j})/2h$.

5.2. **Edge Detection.** In this section, the spatial derivatives in the set of partial differential equations (5) are discretized. After the discretization, the resulting ordinary differential equation in time is solved by the explicit Euler scheme until reaching a steady state. The time interval $(0, T_{fin}]$ is discretized with a time step $\tau = 2.0 \cdot 10^{-6}$. The same approach can be used for equation (4), when neglecting the term g_0. The stopping criteria for both equations are provided in Section 6.

Equation (5) is first integrated over a fixed volume $V_{i,j}$:

$$\int\limits_{V_{i,j}} \frac{\partial \tilde{\psi}}{\partial \theta} = \int\limits_{V_{i,j}} \nabla \tilde{\psi} \cdot \nabla g_0 + \int\limits_{V_{i,j}} |\nabla \tilde{\psi}|_\epsilon g_0 \nabla \left(\frac{\nabla \tilde{\psi}}{|\nabla \tilde{\psi}|_\epsilon} \right). \tag{17}$$

The left-hand side of equation (17) is approximated by $\int\limits_{V_{i,j}} \frac{\partial \tilde{\psi}}{\partial \theta} \approx h^2 \frac{d}{d\theta} \tilde{\psi}\Big|_{x_{i,j}}$.

The first term on the right-hand side of equation (17) is discretized using the first-order upwind scheme. The second term on the right-hand side is discretized using the schemes described in detail in Appendix of [8]. Therefore, the discretization will be described only briefly in this paper. The term is divided into three parts P_1, P_2, P_3:

$$\int\limits_{V_{i,j}} |\nabla \tilde{\psi}|_\epsilon g_0 \nabla \left(\frac{\nabla \tilde{\psi}}{|\nabla \tilde{\psi}|_\epsilon} \right) \approx \underbrace{|\nabla \tilde{\psi}|_\epsilon \Big|_{V_{i,j}}}_{P_1} \underbrace{\frac{1}{1 + K\, |\nabla I|_\epsilon|_{V_{i,j}}}}_{P_2} \underbrace{\int\limits_{V_{i,j}} \nabla \left(\frac{\nabla \tilde{\psi}}{|\nabla \tilde{\psi}|_\epsilon} \right)}_{P_3}.$$

Notation $|\nabla \tilde{\psi}|_\epsilon \Big|_{V_{i,j}}$ and $|\nabla I|_\epsilon|_{V_{i,j}}$, respectively, is used to approximate the values of function $|\nabla \tilde{\psi}|_\epsilon$ and $|\nabla I|_\epsilon$ in the volume element $V_{i,j}$. Similar notation will be used to approximate the value on the edges of these volumes.

The terms P_1, P_2 are discretized as:

$$P_1 \approx \sqrt{\epsilon^2 + \frac{1}{4}\left[\left(|\nabla \tilde{\psi}|_\epsilon \Big|_{E_1} \right)^2 + \left(|\nabla \tilde{\psi}|_\epsilon \Big|_{E_2} \right)^2 + \left(|\nabla \tilde{\psi}|_\epsilon \Big|_{E_3} \right)^2 + \left(|\nabla \tilde{\psi}|_\epsilon \Big|_{E_4} \right)^2 \right]},$$

$$P_2 \approx \frac{1}{1 + K\sqrt{\epsilon^2 + \frac{1}{4}\left[\left(|\nabla I|_\epsilon|_{E_1} \right)^2 + \left(|\nabla I|_\epsilon|_{E_2} \right)^2 + \left(|\nabla I|_\epsilon|_{E_3} \right)^2 + \left(|\nabla I|_\epsilon|_{E_4} \right)^2 \right]}}$$

The discretization of the third term P_3 will be shown on a more general term $\tilde{P}_3 = \int\limits_{V_{i,j}} \nabla \cdot \left(g(\tilde{\psi}) \nabla \tilde{\psi} \right)$, as this approach is used also in the discretization of equations (14) and (15). In the case of term P_3, the function has the form of $g(\tilde{\psi}) = 1/|\nabla \tilde{\psi}|_\epsilon$. First, the Gauss theorem is applied to $\tilde{P}_3$:

$$\tilde{P}_3 = \int\limits_{V_{i,j}} \nabla \cdot \left(g(\tilde{\psi}) \nabla \tilde{\psi} \right) = \int\limits_{S_{i,j}} g(\tilde{\psi}) \nabla \tilde{\psi} \cdot \vec{n}, \tag{18}$$

where $\vec{n}$ denotes the outer unit normal vector to the edge $S_{i,j}$ of the volume $V_{i,j}$. The boundary $S_{i,j}$ consists of four edges E_1, E_2, E_3, E_4 as can be seen in Figure 2.

We substitute the values of normal vectors to the edges:

$$\int_{S_{i,j}} g(\tilde{\psi})\nabla\tilde{\psi}\cdot\vec{n} = \sum_{k=1}^{4}\int_{E_k} g(\tilde{\psi})\nabla\tilde{\psi}\cdot\vec{n} = \int_{E_1}\left[g(\tilde{\psi})\nabla\tilde{\psi}\right]\Big|_{E_1}\cdot(1,0)+$$
$$\int_{E_2}\left[g(\tilde{\psi})\nabla\tilde{\psi}\right]\Big|_{E_2}\cdot(0,-1)+\int_{E_3}\left[g(\tilde{\psi})\nabla\tilde{\psi}\right]\Big|_{E_3}\cdot(-1,0)+\int_{E_4}\left[g(\tilde{\psi})\nabla\tilde{\psi}\right]\Big|_{E_4}\cdot(0,1)$$
$$= \int_{E_1} g(\tilde{\psi})\Big|_{E_1}\frac{\partial\tilde{\psi}}{\partial x}\Big|_{E_1} - \int_{E_2} g(\tilde{\psi})\Big|_{E_2}\frac{\partial\tilde{\psi}}{\partial y}\Big|_{E_2} - \int_{E_3} g(\tilde{\psi})\Big|_{E_3}\frac{\partial\tilde{\psi}}{\partial x}\Big|_{E_3} + \int_{E_4} g(\tilde{\psi})\Big|_{E_4}\frac{\partial\tilde{\psi}}{\partial y}\Big|_{E_4}, \tag{19}$$

where $\frac{\partial\tilde{\psi}}{\partial x}\Big|_{E_i}$ and $\frac{\partial\tilde{\psi}}{\partial y}\Big|_{E_i}$ denote the approximate value of the derivatives on the edges E_i. The final expression (19) is discretized by the scheme described in [8].

5.3. **Signed-Distance Function.** The discretization of the derivatives on the right-hand side of partial differential equation (6) was done by the Godunov scheme [13]. The time interval $(0, T_{fin}]$ is discretized with a time step $\tau = 1.0\cdot 10^{-4}$. The stopping criterion is provided in Section 6.

5.4. **Determining of the Optical Flow.** In order to determine the optical flow field, it is needed to solve the set of partial differential equations (14) and (15). The spatial derivatives are discretized and the resulting system of ordinary differential equation is then solved by the explicit Euler scheme. The time interval $(0, T_{fin}]$ is discretized with time step $\tau = 7.0\cdot 10^{-8}$. The stopping criterion is provided in Section 6.

Equation (14) is first integrated over a fixed volume $V_{i,j}$:

$$\int_{V_{i,j}}\frac{\partial u_1}{\partial\theta} = -\alpha\int_{V_{i,j}}\left(\frac{\partial\phi}{\partial x}u_1+\frac{\partial\phi}{\partial y}u_2+\frac{\partial\phi}{\partial t}\right)\frac{\partial\phi}{\partial x}+$$
$$\beta\int_{V_{i,j}}\nabla\cdot\left(q'(\|\nabla u_1\|^2+\|\nabla u_2\|^2)\nabla u_1\right)-\gamma\int_{V_{i,j}}u_1.$$

The left-hand side is approximated by $\int_{V_{i,j}}\frac{\partial u_1}{\partial\theta}\approx h^2\frac{d}{d\theta}u_{1,i,j}$. The first term on the right-hand side is approximated by $\int_{V_{i,j}}\left(\frac{\partial\phi}{\partial x}u_1+\frac{\partial\phi}{\partial y}u_2+\frac{\partial\phi}{\partial t}\right)\frac{\partial\phi}{\partial x}\approx h^2\left(\phi_{x;i,j}u_{1,i,j}+\phi_{y;i,j}u_{2,i,j}+\phi_{t;i,j}\right)\overline{\phi}_{x;i,j}$ and the third one as $\int_{V_{i,j}}u_1\approx h^2u_{1,i,j}$.

The second term on the right-hand side, $\int_{V_{i,j}}\nabla\cdot(q'\nabla u_1)$, has the same form as the term (18) and it is discretized in the same way.

6. **Experimental Results.** In the beginning of this section we introduce the notation, norms and functions used to evaluate the results of registration and the stopping criteria for equations discretized in the previous section. Then, we present the results of the proposed method applied on synthetic and real heart MOLLI images. The results are compared with the mutual information maximization method

[9], for which the version described in [21] and implemented in MIRTK library[1] was used.

Mutual information is a widely used metrics for comparing multimodality medical images. In the following section, the normalized mutual information will be used to evaluate the difference between the images with varying intensity. Before its definition, we introduce the following notations. Let $P(i)$ denote the probability of intensity i in image I with the range of discrete intensities $\{0, 1, .., i_{\max}\}$. For two images I, J, $P(i, j)$ denotes joint probability of intensities i, j being present at the same position in images I, J. For the given images and intensity ranges, these probabilities can be computed based on histograms. The normalized mutual information is defined in the following way: $MI(I, J) = (H(I) + H(J))/H(I, J)$, where $H(I) = -\sum_{i=0}^{i_{\max}} P(i)\ln(P(i))$ denotes the marginal entropy of given image and $H(I, J) = -\sum_{i,j=0}^{i_{\max}} P(i, j)\ln(P(i, j))$ denotes the joint entropy of two images.

For the difference between the signed-distance functions the following norm will be used: $\|\phi_1 - \phi_2\|_2 = \left(\sum_{i=1,j=1}^{N_1,N_2} (\phi_1(x_{i,j}) - \phi_2(x_{i,j}))^2\right)^{\frac{1}{2}}$. The same formula can be applied to level-set functions and image functions I_1, I_2 of binary images.

In the following subsections, the target image is denoted as T, the source image by S and the signed-distance functions of the target and source objects by ϕ_T and ϕ_S, respectively. The source image registered by the given method is denoted by S_{method}, the registered signed-distance function of source object by $\phi_{S,method}$. The compared methods include: optical flow applied to signed-distance functions (OF^{dist}), mutual information maximization method applied to the original images (MIM) and to the signed-distance functions (MIM^{dist}). The stopping criteria and values of T_{fin} used to generate the presented results are as follows. The condition $\frac{\|\tilde{\psi}^{n+1} - \tilde{\psi}^n\|_2}{\|\psi^n\|_2} < 5 \cdot 10^{-4}$ was used as a stopping criterion for edge-detection equation. The equation used for image de-noising is not solved until a steady state to avoid "over-smoothing" of the image, hence T_{fin} was set to $6 \cdot 10^{-5}$. The distance function was evaluated only in the surroundings of the zero level set. Therefore, based on [22], it is not necessary to solve the equation until reaching the steady state. In order to get correct solution in the 10-pixel-wide neighborhood of the zero level set, it was sufficient to set $T_{fin} = 10h$. For the optical flow equation, the stopping condition was used in a form $\frac{\|u_1^{n+1} - u_1^n\|_2 + \|u_2^{n+1} - u_2^n\|_2}{\|u_1^n\|_2 + \|u_2^n\|_2} < 0.002$.

6.1. **Synthetic images with single object.** Two binary synthetic images with one fully visible object are shown in Figures 3a and 3b. Thanks to the simplicity of the scene, the segmentation was done by thresholding. The OF^{dist} method was applied to the signed-distance functions, as described in the previous sections. To provide a relevant comparison, the mutual information maximization method was applied directly to the images and to the signed-distance functions (i.e. methods MIM and MIM^{dist}).

The absolute value of the difference between the target and source images before registration can be seen in Figure 3c. The differences after registration by OF^{dist}, MIM and MIM^{dist} are shown in the second line of Figure 3. As can be seen in Table 1, the best result was obtained by the MIM method. The segmentation of the object of interest does not provide any advantage in this case.

[1] `https://mirtk.github.io/sidebar.html`

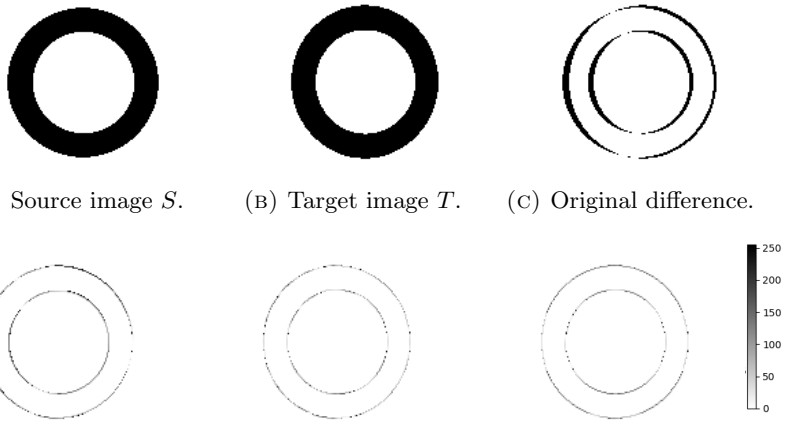

(A) Source image S. (B) Target image T. (C) Original difference.

(D) Difference between $S_{OF^{dist}}$ and T. (E) Difference between S_{MIM} and T. (F) Difference between $S_{MIM^{dist}}$ and T.

FIGURE 3. Source image (A), target image (B), the absolute value of their difference before registration (C) and after registration by OF^{dist}, MIM and MIM^{dist} (D-F). Parameters of OF^{dist}: $N_1 = 200, N_2 = 200, \alpha = 1.0, \beta = 3.25, \gamma = 2.5$.

$\|T - S\|_2$	$\|T - S_{OF^{dist}}\|_2$	$\|T - S_{MIM}\|_2$	$\|T - S_{MIM^{dist}}\|_2$
9462.47	3130.83	2173.93	2607.66

TABLE 1. Norms of difference between the target 3b image and source image 3a before and after registration by OF^{dist}, MIM and MIM^{dist}.

6.2. **Synthetic images with two objects.** Next, we present binary synthetic images with two fully visible objects. The source and target images are shown in Figures 4a and 4b, respectively. The absolute value of the difference between the target and source images before registration can be seen in Figure 4c.

First, both objects were registered by OF^{dist}, MIM and MIM^{dist}. The differences between the source and target image after registration are presented in the second line of Figure 4. The direct application of MIM is not suitable in this case, as can be seen in Figure 4e. Much better results were obtained by the MIM^{dist} method, which uses the signed-distance functions. However, as the values in Table 2 show, the smallest error was obtained by OF^{dist}. In Figure 5 the difference between OF^{dist} and MIM^{dist} approach is well visible. Applying MIM^{dist} decreases the error uniformly throughout the whole image (Figure 5b), while OF^{dist} (Figure 5b) creates unevenly distributed error. Similar results could be expected for a larger number of fully visible objects.

In the next experiment, one object was segmented (marked by a green line in Figure 6a) and registered by OF^{dist}, while MIM was applied directly on the images in order to provide global registration. The results can be seen in Figures 6b and 6c, respectively. The global registration by MIM provides smaller global error, as can be seen in Table 4. However, the local registration by OF^{dist} (denoted by $S_{1,OF^{dist}}$) provides smaller error in the object of interest as can bee seen in Figure 6.

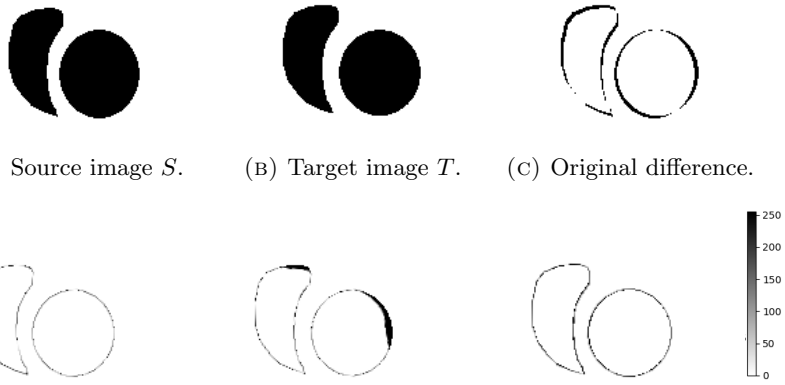

(A) Source image S. (B) Target image T. (C) Original difference.

(D) Difference between $S_{OF^{dist}}$ and T. (E) Difference between S_{MIM} and T. (F) Difference between $S_{MIM^{dist}}$ and T.

FIGURE 4. Source image (A), target image (B) and the absolute value of their difference before (C) and after registration by OF, MIM and MIM^{dist} (D-F). Parameters of OF^{dist}: $N_1 = 200, N_2 = 200, \alpha = 1.5, \beta = 3.75, \gamma = 3.25$.

$\|T - S\|_2$	$\|T - S_{OF^{dist}}\|_2$	$\|T - S_{MIM}\|_2$	$\|T - S_{MIM^{dist}}\|_2$
6654.44	2199.07	4121.95	3602.27

TABLE 2. Norms of difference between the target image in Figure 4b image and source image in Figure 4a before and after registration by OF^{dist}, MIM and MIM^{dist}.

$\|\phi_T - \phi_S\|_2$	$\|\phi_T - \phi_{S,OF^{dist}}\|_2$	$\|\phi_T - \phi_{S,MIM^{dist}}\|_2$
0.849915	0.239367	0.2950385

TABLE 3. Norms of difference between target and source signed-distance function before and after registration by OF^{dist} and MIM. The source and target objects can be seen in Figure 4a and 4b, respectively.

$\|T - S\|_2$	$\|T - S_{1,OF^{dist}}\|_2$	$\|T - S_{MIM}\|_2$
6654.44	5062.1	4121.95

TABLE 4. Norms of difference between the target image 4b and source image 4a before registration, after registration of one object by OF^{dist}, and after global registration by MIM.

6.3. **Results on real data.** In this section, we present a comparison of the three registration approaches on real MRI MOLLI data. A set of three images with segmented myocardium marked by the green contour is presented in Figure 7. In this case, the segmentation was done by the level-set method described in Section 5.2. The initial circle around the segmented object was provided by the user. The initial

(A) Difference between ϕ_T and ϕ_S . (B) Difference between ϕ_T and $\phi_{S,OF^{dist}}$. (C) Difference between ϕ_T and $\phi_{S,MIM^{dist}}$.

FIGURE 5. Absolute value of the difference between the target and source signed-distance function before and after registration by OF^{dist} and MIM^{dist}. The signed-distance functions are computed on 10-pixel-wide neighborhood of the edges of the object and set to constant outside the neighborhood.

(A) The segmented object. (B) Difference between T and $S_{OF^{dist}}$. (C) Difference between T and S_{MIM}.

FIGURE 6. The results of OF^{dist} registration of object marked by green line in 6a, and global MIM registration of the whole scene.

level-set function with properties given by (1) was then computed as $\psi_0(x_{i,j}) = \|x_{i,j} - s\| - r$, where s is the center of the circle and r is the radius. The values of parameter K, which governs the sensitivity of edge detection in equation (5), are provided in the caption of Figure 7.

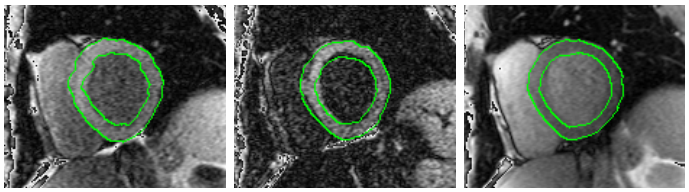

(A) Source mage S_1. (B) Source image S_2. (C) Target image T.

FIGURE 7. Images from the MOLLI sequence with segmented myocardium. Parameters for the outer edge detection: $K_{S_1} = 1.3 \cdot 10^{-6}$, $K_{S_2} = 1.3 \cdot 10^{-6}$, $K_T = 2.3 \cdot 10^{-6}$. Parameters for the inner edge detection: $K_{S_1} = K_{S_2} = K_T = 9.0 \cdot 10^{-6}$.

The images were registered by OF^{dist}, MIM and MIM^{dist}. The results of all these approaches are presented in Figure 8.

MI measure was used to compare all three registration approaches. The MI was computed only in a 10-pixels-wide surroundings of the edge of the segmented object. The values of MI are presented in Table 5. The largest increase of MI was

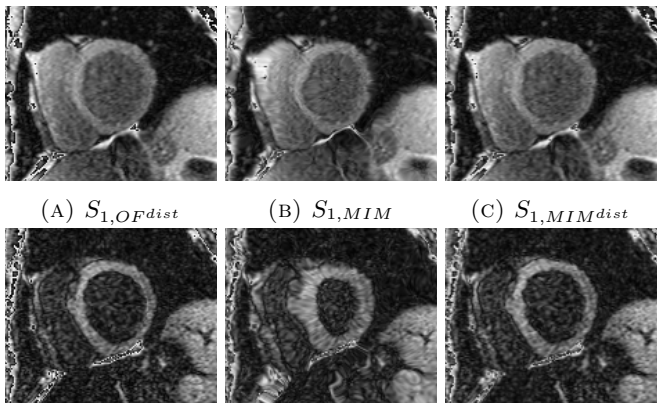

(A) $S_{1,OF^{dist}}$ (B) $S_{1,MIM}$ (C) $S_{1,MIM^{dist}}$

(D) $S_{2,OF^{dist}}$ (E) $S_{2,MIM}$ (F) $S_{2,MIM^{dist}}$

FIGURE 8. Results of registration of S_1, S_2 with target image T. Parameters of OF^{dist}: $N_1 = 256, N_2 = 218, \alpha = 1.25, \beta = 3.5, \gamma = 3.0$.

i	$MI(T, S_i)$	$MI(T, S_{i,OF^{dist}})$	$MI(T, S_{i,MIM})$	$MI(T, S_{i,MIM^{dist}})$
1	1.1556	1.2184	1.2273	1.2170
2	1.1012	1.2034	1.2052	1.1964

TABLE 5. MI target image and source images from Figure 8 before and after registration by OF and MIM and MIM^{dist}. The MI was computed only in the surroundings of the segmented objects.

obtained by direct application of MIM on the source and target images. However, the transformation led to deformation of the myocardium, as can be seen especially in Figure 8e. The results obtained by OF^{dist} and MIM^{dist} are visually comparable. The unrealistic deformation of the myocardium is avoided when using the signed-distance function (see Figures 8d and 8f), while the value of mutual information is higher. The largest increase of mutual information was obtained by the OF^{dist} method.

A software for the registration of series with varying image intensity function, using the proposed method, can be found on
`http://geraldine.fjfi.cvut.cz/mmg-medical-tools`.

7. **Conclusion.** This paper presented an approach to the registration of medical images with varying image intensity. We were specifically interested in the MOLLI-image series, in which the changes in intensity and contrast make the registration challenging. The proposed registration method consists of the segmentation of the object of interest by level set method, its representation by a signed-distance function and determining optical flow based on this functions. The transformation between source and target signed-distance function is then applied to the original images.

The proposed method (OF^{dist}) was compared with two traditional registration methods based on maximization of mutual information: either applied to the original images (MIM) or to the signed-distance function (MIM^{dist}). The experiments

on synthetic binary images with one or two objects and on real images of the MOLLI cardiac MRI sequence were presented. The segmentation of the object of interest provided no advantage in the case of one binary object. It was however proven to be beneficial in other tested cases, i.e. synthetic image with two objects of interest or the images of real MOLLI sequence, where both OF^{dist} and MIM^{dist} provided better results than MIM. In particular, in the experiments on real MOLLI images the MIM provided the largest increase in mutual information by prioritizing the registration of more distinct objects in the scene. This, however, led to unrealistic deformation of the myocardium, which was then avoided by using OF^{dist} and MIM^{dist}. Based on the experiments, it can be concluded, that the proposed segmentation-based registration using the signed-distance function provides better results when registering the objects of interest which are not the most distinct in the scene.

Acknowledgement. This work was supported by the Ministry of Education, Youth and Sports of the Czech Republic under the OP RDE grant number CZ.02.1.01/0.0/0.0/16_019/0000778 "Centre for Advanced Applied Sciences" and by project No. 15-27178A of Ministry of Health of the Czech Republic. This work was in addition partially supported by the Inria-UT Southwestern Associated Team TOFMOD. The authors also acknowledge a financial support from the Department of Health through the National Institute for Health Research (NIHR) comprehensive Biomedical Research Centre award to Guy's & St Thomas' NHS Foundation Trust in partnership with King's College London and the NIHR Cardiovascular MedTech Co-operative (previously Cardiovascular Healthcare Technology Co-operative 2012– 2017), and the support of Wellcome/EPSRC Centre for Medical Engineering [WT 203148/Z/16/Z]. The views expressed are those of the author(s) and not necessarily those of the NHS, the NIHR or the Department of Health.

REFERENCES

[1] V. Caselles, R. Kimmel and G. Sapiro, Geodesic active contours, in *Computer Vision, 1995. Proceedings., Fifth International Conference on*, IEEE, 1995, 694–699.

[2] L. C. Evans, J. Spruck et al., Motion of level sets by mean curvature., *Journal of Differential Geometry*, **33** (1991), 635–681.

[3] M. A. Fischler and R. A. Elschlager, The representation and matching of pictorial structures, *IEEE Transactions on computers*, **100** (1973), 67–92.

[4] I. M. Gelfand, R. A. Silverman et al., *Calculus of variations*, Courier Corporation, 2000.

[5] A. Handlovičová, K. Mikula and F. Sgallari, Semi-implicit complementary volume scheme for solving level set like equations in image processing and curve evolution, *Numerische Mathematik*, **93** (2003), 675–695.

[6] B. K. Horn and B. G. Schunck, Determining optical flow, *Artificial intelligence*, **17** (1981), 185–203.

[7] J. Jost, *Postmodern analysis*, Springer Science & Business Media, 2006.

[8] V. Klement, T. Oberhuber and D. Ševčovič, Application of the level-set model with constraints in image segmentation, *Numerical Mathematics: Theory, Methods and Applications*, **9** (2016), 147–168.

[9] F. Maes, A. Collignon, D. Vandermeulen, G. Marchal and P. Suetens, Multimodality image registration by maximisation of mutual information, *IEEE transactions on Medical Imaging*, **16** (1997), 187–198.

[10] J. A. Maintz and M. A. Viergever, A survey of medical image registration, *Medical image analysis*, **2** (1998), 1–36.

[11] T. Makela, P. Clarysse, O. Sipila, N. Pauna, Q. C. Pham, T. Katila and I. E. Magnin, A review of cardiac image registration methods, *IEEE Transactions on medical imaging*, **21** (2002), 1011–1021.

[12] S. Osher and J. A. Sethian, Fronts propagating with curvature-dependent speed: Algorithms based on Hamilton-Jacobi formulations, *Journal of computational physics*, **79** (1988), 12–49.

[13] D. Peng, B. Merriman, S. Osher, H. Zhao and M. Kang, A PDE-based fast local level set method, *Journal of computational physics*, **155** (1999), 410–438.
[14] P. Perona and J. Malik, Scale-space and edge detection using anisotropic diffusion, *IEEE Transactions on pattern analysis and machine intelligence*, **12** (1990), 629–639.
[15] G. Peyré, M. Péchaud, R. Keriven, L. D. Cohen et al., Geodesic methods in computer vision and graphics, *Foundations and Trends® in Computer Graphics and Vision*, **5** (2010), 197–397.
[16] R. Precup, *Methods in nonlinear integral equations*, Springer Science & Business Media, 2013.
[17] J. A. Sethian et al., Numerical algorithms for propagating interfaces: Hamilton-Jacobi equations and conservation laws, *Journal of differential geometry*, **31** (1990), 131–161.
[18] J. A. Sethian, *Level Set Methods: Evolving Interfaces in Geometry, Fluid Mechanics, Computer Vision, and Materials Scie*, Cambridge university press, 1996.
[19] T. W. Tang and A. C. Chung, Non-rigid image registration using graph-cuts, in *International Conference on Medical Image Computing and Computer-Assisted Intervention*, Springer, 2007, 916–924.
[20] S. Chen, A. Rahman, Contrast enhancement using recursive mean-separate histogram equalisation for scalable brightness preservation, *IEEE Transactions on consumer Electronics*, **49** (2003), 1301–1309
[21] D. Rueckert, L. I. Sonoda, C. Hayes, D. L. Hill, M. O. Leach, and D. J. Hawkes, "Nonrigid registration using free-form deformations: application to breast MR images," *IEEE transactions on medical imaging*, vol. 18, no. 8, pp. 712–721, 1999.
[22] J. F Aujol and G. Aubert, Signed distance functions and viscosity solutions of discontinuous Hamilton-Jacobi Equations *INRIA Res. Rep*, 4507 (2002)

Received xxxx 20xx; revised xxxx 20xx.

E-mail address: katerina.skardova@fjfi.cvut.cz
E-mail address: tomas.oberhuber@fjfi.cvut.cz
E-mail address: jaroslav.tintera@medicon.cz
E-mail address: radomir.chabiniok@inria.fr